applied optics

Staircase-scene-based nonuniformity correction in aerial point target detection systems

Lijun Huo,[1,2,3] Dabiao Zhou,[1,2,3] Dejiang Wang,[2,3,*] Rang Liu,[1,2,3] and Bin He[2]

[1]University of Chinese Academy of Sciences, Beijing 100049, China
[2]Changchun Institute of Optics, Fine Mechanics and Physics, Chinese Academy of Sciences, Changchun, Jilin 130033, China
[3]Key Laboratory of Airborne Optical Imaging and Measurement, Changchun Institute of Optics, Fine Mechanics and Physics, Chinese Academy of Sciences, Changchun, Jilin 130033, China
*Corresponding author: wangdj04@ciomp.ac.cn

Received 2 June 2016; revised 18 July 2016; accepted 9 August 2016; posted 10 August 2016 (Doc. ID 267628); published 31 August 2016

Focal-plane arrays (FPAs) are often interfered by heavy fixed-pattern noise, which severely degrades the detection rate and increases the false alarms in airborne point target detection systems. Thus, high-precision nonuniformity correction is an essential preprocessing step. In this paper, a new nonuniformity correction method is proposed based on a staircase scene. This correction method can compensate for the nonlinear response of the detector and calibrate the entire optical system with computational efficiency and implementation simplicity. Then, a proof-of-concept point target detection system is established with a long-wave Sofradir FPA. Finally, the local standard deviation of the corrected image and the signal-to-clutter ratio of the Airy disk of a Boeing B738 are measured to evaluate the performance of the proposed nonuniformity correction method. Our experimental results demonstrate that the proposed correction method achieves high-quality corrections.

OCIS codes: (100.2550) Focal-plane-array image processors; (040.2480) FLIR, forward-looking infrared; (110.3080) Infrared imaging; (010.5630) Radiometry; (110.4280) Noise in imaging systems.

http://dx.doi.org/10.1364/AO.55.007149

1. INTRODUCTION

Infrared (IR) point target detection is one of the most crucial techniques in the IR search and track (IRST) surveillance system, which possesses night vision, anti-hidden capability, and mist-penetrating power. Point targets are inevitably interfered by heavy noises, including temporal noise and spatial noise. The fixed-pattern noise is the major spatial noise, which is due to detector-to-detector variation from the same input and nonuniformity in the readout and digitization circuitry. The diffraction spot of a long-distance target occupies not more than 3×3 pixels in the focal-plane array (FPA), and a poor nonuniformity correction (NUC) accounts for high false alarms and close range in point target detection systems [1,2]. In turn, a high-precision NUC method, taking into account the entire imaging system from the lens to the digital data, is needed.

Over the past few decades, several methods have been proposed, and they can be broadly classified into two major categories. The first category is calibration-based techniques, such as the two-point calibration algorithm, which employs uniform calibration sources, and where all the pixels of the FPA are mapped linearly to the average response [3]. A more accurate correction result can be obtained by this type of technique. Compared with visible and near-infrared sensors, long-wave infrared (LWIR) sensors are less stable, and the nonuniformity tends to drift slowly with time. Besides, as the temperature changes a lot with altitude change, it takes a long time to reach temperature equilibrium between the aerial camera interior and ambiance, during which the shape of the camera lens may change. In addition, the fluctuation of atmospheric pressure may induce changes. These factors severely degrade the effectiveness of the one-time laboratory-derived NUC. Unlike general visualization applications, airborne IRST systems achieve a high-precision NUC at the expense of a repeated in-flight calibration, which means the imaging operation must be halted. In practice, a mechanical system is required to switch a reflector or an internal blackbody into the optical path [4,5]. There are several problems with this approach. In IRST systems, the optical systems are often designed to have a large aperture to enhance the detection ability. Thus, it is impractical to calibrate the entire optical system with a blackbody of the same size as the primary lens, given the limited space and weight restriction for aerial equipment. In other words, the in-flight calibration remains an inner calibration. Furthermore, the response of nonlinear sensors may require a higher-order relationship [6]. The precision of the two-point calibration may decrease when the scene temperature drifts away from the calibration point.

The second category is scene-based techniques. Constant-statistics-based algorithms make use of similar statistics of

individual detectors and restrict statistical parameters to a predefined reference [7–9]. Least mean square algorithms deduce the NUC parameters with an estimation of the true irradiance image [10,11]. Registration-based algorithms rely on the assumption that different pixels should respond similarly for the same scene point, which may experience the difficulty of accurate registration over a large expanse of the sky with rapidly changing clouds [12–14]. The most commonly used method utilizes approximately uniform scenes, such as fields or open water. However, it may be impossible for aerial IRST systems to find a uniformly distributed scene. The temperature of the troposphere increases with the decrease of altitude due to earth surface radiation, and the scene correspondingly intensifies perpendicular to the scanning direction. That is, the scene is presented with the staircase effect.

In this paper, we investigate the use of a staircase scene to build a new NUC method for airborne point target detection systems. Besides the superior computational efficiency, the entire optical system is corrected without halting the process of normal imaging. Moreover, as the to-be-corrected temperature scene matches the referenced staircase scene, the proposed method can compensate for the response nonlinearity of the detector.

This paper is organized as follows. In Section 2, we review the standard two-point calibration method, and then describe the proposed NUC method based on staircase scenes. Section 3 presents experimental results on real images, and discusses the effect of the proposed method on the signal-to-clutter ratio (SCR) of the target. Finally, summarizations and conclusions are presented in Section 4.

2. NUC MODEL

A. Observation Model

In this paper, the output gray value is assumed to be linear, which can be modeled as

$$I_{i,j} = G_{i,j} \cdot E_{i,j} + O_{i,j}, \tag{1}$$

where $I_{i,j}$ is the gray value of the (i,j)th pixel of output image I in units of digital number (DN). Here, subscripts i and j index the row and column number, respectively. The coordinate origin is on the top left. $E_{i,j}$ is the energy incident on the (i,j)th pixel during the integration time t. $G_{i,j}$ is the response in units of DN/(W · s). $O_{i,j}$ is the offset, which is the sum of the reflected ambient radiation flux, the stray radiation flux, and the internal factors of the detector, for instance, the dark current and the readout circuitry.

For an ideal blackbody with temperature T, the energy that strikes each detector element is equal to $E(T)$, given by

$$E(T) = t \cdot \frac{\pi \cdot \epsilon \tau_{\text{opt}}}{4} \cdot \left(\frac{D}{f}\right)^2 \cdot A_d \cdot L(T), \tag{2}$$

where τ_{opt} and D are the transmittance and diameter of the optics, respectively. Here, f denotes the focal length, and A_d denotes the sensitive area of a detector element. ϵ is the emissivity of the blackbody. $L(T)$ represents the radiance of an ideal blackbody at temperature T [15]. For a given IR system, the nonuniformity stems from the variation of $G_{i,j}$ and $O_{i,j}$ of different pixels in FPAs.

B. Standard Two-Point Calibration Method

The simplest method to correct the nonuniformity is to perform measurements with a blackbody at two different absolute temperatures T_1 and T_2, and then solve for the calibration coefficients $k_{i,j}$ and $b_{i,j}$ [3,5]. That is,

$$\begin{cases} k_{i,j} I_{1,i,j} + b_{i,j} = \overline{I_1} \\ k_{i,j} I_{2,i,j} + b_{i,j} = \overline{I_2} \end{cases}. \tag{3}$$

Here, I_1 and I_2 are the acquired images when the blackbody temperature is T_1 and T_2, respectively. $\overline{I_1}$ and $\overline{I_2}$ are the mean values of images I_1 and I_2, and $\overline{G}$ and $\overline{O}$ are the average response and offset of all the detector elements. These parameters are calculated in detail in Appendix A.

Solving Eq. (3) yields

$$\begin{cases} k_{i,j} = \frac{\overline{G}}{G_{i,j}} \\ b_{i,j} = \overline{O} - \frac{\overline{G}}{G_{i,j}} O_{i,j} \end{cases}. \tag{4}$$

However, as presented in Subsection 3.A, when the temperature of the to-be-calibrated scene is far away from calibration points T_1 and T_2, the standard deviation (STD) of the corrected image may increase. This is attributed to the fact that the response of the detector is not perfectly linear, and Eq. (1) is just an approximation to a high-order polynomial [6,16].

In airborne IRST systems, the camera sweeps out overlapping images in circles with a fixed pitch angle. Unlike general imaging systems where the images have a high dynamic range and may contain abundant textures, the images from airborne IRST systems are filled with sky and no grounds. The dynamic range of these images is relatively stable in a given area, and the intensities may increase with the row index as a characteristic of atmospheric temperature. The gray values of the first row and the last row may differ significantly. In the standard two-point calibration method, an appropriate choice of the temperature of the blackbody may be the average temperature of the scene [5]. However, this may decrease the nonuniformity precision in the rows where the intensity values are far away from average value. A natural solution is employing a "staircase blackbody," of which the temperature matches the scene row by row. This motivates us to calibrate the scene against a sky background by a staircase blackbody, which is defined as

$$E'_{2,i} = E_2 + \Delta E_i, \tag{5}$$

where $E'_{2,i}$ is the energy incident on the pixels in the ith row. That is, E'_2 appears uniform in the row direction and we see the staircase effect in the column direction.

C. NUC Based on Staircase Blackbody

Let I'_2 be the image corresponding to the staircase blackbody. Similarly, to solve for calibration coefficients $k'_{i,j}$ and $b'_{i,j}$, replace I_2 with I'_2; then rewrite Eq. (3) as

$$\begin{cases} k'_{i,j} I_{1,i,j} + b'_{i,j} = \overline{I_1} \\ k'_{i,j} I'_{2,i,j} + b'_{i,j} = \overline{I'_2} \end{cases}, \tag{6}$$

where $\overline{I'_2}$ is the mean value of image I'_2. As deduced in Appendix A, coefficient $k'_{i,j}$ takes the following form:

$$k'_{i,j} = \frac{\overline{G}}{G_{i,j}} + \frac{\frac{1}{M}\sum_{m=1}^{M}\left(\frac{1}{N}\sum_{n=1}^{N} G_{m,n}\right)(\Delta E_m - \Delta E_i)}{G_{i,j}(E_2 - E_1 + \Delta E_i)}. \quad (7)$$

The average response of all the N detector elements in row m is denoted by $\overline{G_m}$ as follows:

$$\overline{G_m} = \frac{1}{N}\sum_{n=1}^{N} G_{m,n} \approx \overline{G}. \quad (8)$$

For analysis simplification, it is reasonable to approximate $\overline{G_m}$ by $\overline{G}$, since $G_{i,j}$ is a randomly distributed variable with the average $\overline{G}$, which will be further demonstrated in Subsection 3.B. Substituting Eq. (8) into (7) yields

$$k'_{i,j} = \frac{\overline{G}}{G_{i,j}}\left[1 + \frac{\frac{1}{M}\sum_{m=1}^{M}(\Delta E_m - \Delta E_i)}{E_2 - E_1 + \Delta E_i}\right]. \quad (9)$$

To simplify the notation, denote that

$$s_i = \frac{\frac{1}{M}\sum_{m=1}^{M}(\Delta E_m - \Delta E_i)}{E_2 - E_1 + \Delta E_i}. \quad (10)$$

Further, rewrite Eq. (9) as

$$k'_{i,j} = k_{i,j}(1 + s_i). \quad (11)$$

Similarly, coefficient $b'_{i,j}$ takes the following form:

$$b'_{i,j} = b_{i,j} - s_i \cdot \overline{G}\left(E_1 + \frac{O_{i,j}}{G_{i,j}}\right). \quad (12)$$

D. Discussion

Compared to the standard two-point calibration method, it is obvious that $k'_{i,j}$ is proportional to the scale factor $(1 + s_i)$, and that $b'_{i,j}$ is added by an offset $[-s_i \cdot \overline{G}(E_1 + O_{i,j}/G_{i,j})]$. The dependence of $k'_{i,j}$ on s_i results in two effects: on the one hand, for the ith row, i is a fixed number and the scale factor $(1 + s_i)$ remains constant. As a consequence, $k'_{i,j}$ follows the same trend as $k_{i,j}$. On the other hand, for the jth column, i ranges from 1 to M; thus $k'_{i,j}$ keeps changing with both s_i and $k_{i,j}$.

To analyze the monotonicity of s_i, assume that $E_2 > E_1$ and $i_2 > i_1$ without loss of generality. As deduced in Appendix A, s_i keeps decreasing with the increase of index i when $\Delta E_{i_2} > \Delta E_{i_1}$, and s_i keeps increasing when $\Delta E_{i_2} < \Delta E_{i_1}$. Thus, in general, $k'_{i,j}$ keeps decreasing with the increase of i when $\Delta E_{i_2} > \Delta E_{i_1}$, and vice versa. As a factor $(-s_i)$ is included in the coefficient $b'_{i,j}$, it follows an opposite trend to $k'_{i,j}$. Figure 1 is the diagram of the proposed method.

There are two practical concerns of the proposed method. The first concern is that the proposed method is relatively accurate but inaccurate in absolute. In other words, the method is only accurate within narrow dynamic range; i.e., the intensities of all the rows are corrected to the average intensity of the reference image. We might restore the NUC coefficients linearly tapping into the prior knowledge that $k_{i,j}$ is around 1 and $b_{i,j}$ is around 0. In such a case, this method is enough for point target detection systems, since the target occupies not more than 3×3 pixels and only local spatial processing is primarily needed. The second concern is that it may be labor-intensive and impossible to find a scene that is uniform in each row in extreme weather. If the nonuniform area is small, it may be most practical to replace the NUC coefficients of the polluted sections [16]. On the other hand, if the scene is full of nonuniform areas, i.e., heavy clouds, the previous NUC coefficients may have similar performance for the point target systems. Thus, it may be a good choice not to update the current NUC coefficients under extreme weather [16].

3. EXPERIMENTS

To validate the NUC performance, we experimented with a mercury cadmium telluride LWIR detector with a Stirling cycle cooler manufactured by Sofradir. The parameters of the detector and optics of the tested IR imaging system are condensed in Table 1. The noise equivalent difference temperature (NEDT) of the FPA was given for a 300 K scene temperature with the integration time of 250 μs.

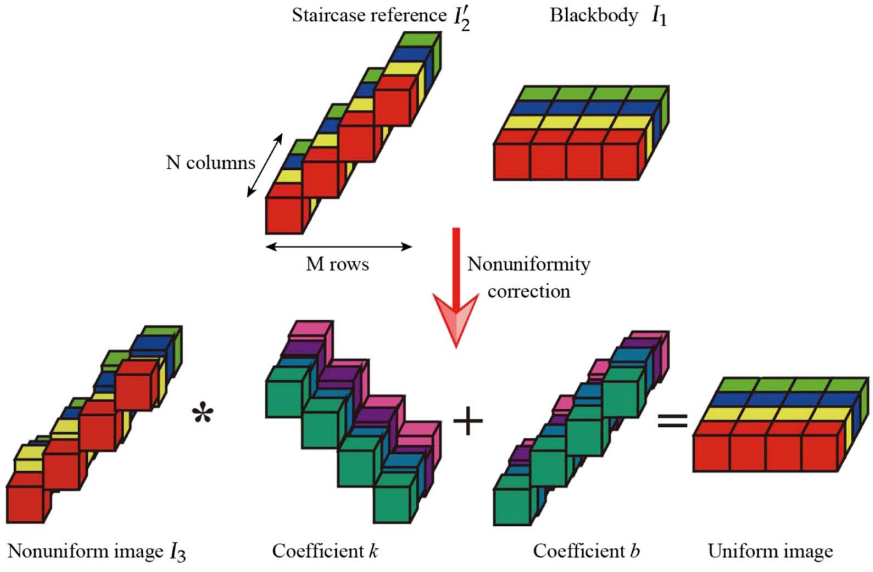

Fig. 1. Diagram of the NUC method based on staircase scenes when $E_2 > E_1$ and $\Delta E_{i_2} > \Delta E_{i_1}$.

Table 1. Detailed Features of the Tested IR System

Parameter	Value
Spectral band pass (μm)	7.7–11.3
Native resolution	320 × 256
Pixel size (μm)	30
NEDT (mK)	19
Camera output resolution (bit)	14
Operating temperature (K)	77
Full frame rate (f/s)	100
Focal length (mm)	38
$F/\#$	2
FOV (deg.)	14.40 × 11.54

A. Laboratory Calibration

The practical experimental devices are illustrated in Fig. 2. A CI blackbody was employed to provide an even radiant flux. The FPA with imaging lens and driving circuits was mounted onto the optics vibration platform. The captured images were transmitted to a Teledyne DALSA frame grabber inside the personal computer (PC) through a Camera Link Interface. The integration time was set to 200 μs through the serial port.

The temperature of the to-be-calibrated scene is T_3. The corresponding image is I_3. We perform the standard two-point calibration experiment with the blackbody in two scenarios: (1) T_1 is fixed to 285 K and $T_2 \in \{288\text{ K}, 289\text{ K}, 290\text{ K}, 291\text{ K}\}$. T_3 ranges from 289 to 311 K. (2) T_1 is fixed to 285 K and $T_3 \in \{288\text{ K}, 289\text{ K}, 290\text{ K}, 291\text{ K}\}$. T_2 ranges from 289 to 311 K. The corresponding radiance to blackbody temperature {288 K, 289 K, 290 K, 291 K} is $\{28.06, 28.58, 29.11, 29.64\}\text{W} \cdot \text{cm}^{-2}$. Since relative errors are of more concern in point detection systems, we refer to the global STD, rather than the mean absolute error, to quantitatively assess the residual nonuniformity. The STD of the calibrated images of the two scenarios is shown in Fig. 3.

In Scenario 1, it is illustrated in Fig. 3(a) that the global STD increases when temperature T_3 is away from the calibration points T_1 and T_2 due to the nonlinear response of the detector. It indicates that the scene should be calibrated with a blackbody of a temperature that matches the scene temperature. Besides, when $T_1 = T_3 = 288$ K, the global STD is 5.6 rather than 0, which is due to the differences between the random noises of I_1 and of I_3. In scenario 2, we can see from Fig. 3(b) that the global STD rises with the increase of calibration point T_2. However, as T_2 continues to rise, the further attainable global STD augmenter is quite limited. It reveals that for the two-point calibration method, as long as T_3 is near T_1 or T_2, the global STD can be controlled below a value of 7. This further demonstrates the rationale of replacing only one of the uniform scenes with a staircase scene, of which the temperature exactly matches that of the scene in a row-wise manner.

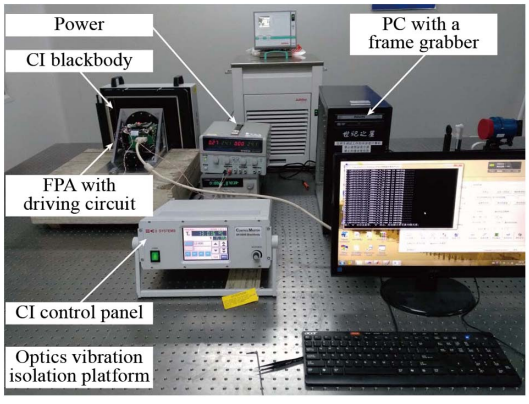

Fig. 2. Practical FPA calibration platform.

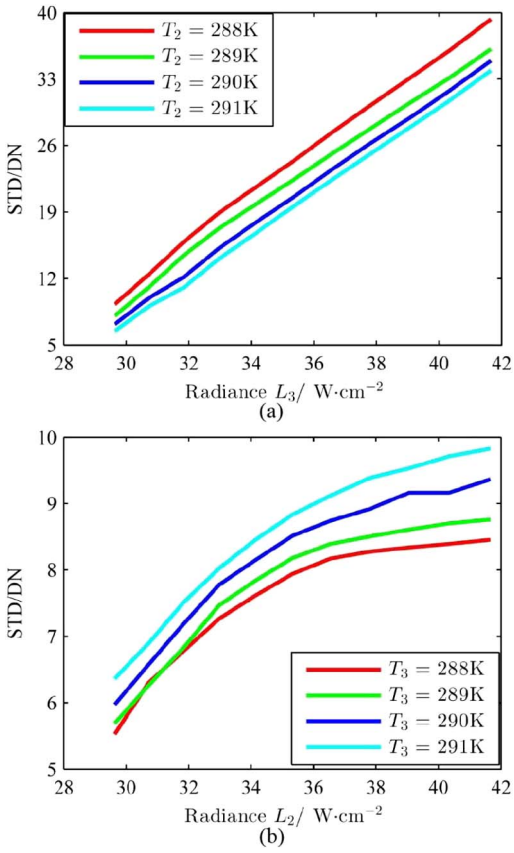

Fig. 3. Global STD of the calibrated image as a function of the blackbody radiance. (a) Scenario 1: $T_1 = 285$ K, $T_2 \in \{288\text{ K}, 289\text{ K}, 290\text{ K}, 291\text{ K}\}$, and $T_3 \in [289\text{ K}, 311\text{ K}]$. (b) Scenario 2: $T_1 = 285$ K, $T_3 \in \{288\text{ K}, 289\text{ K}, 290\text{ K}, 291\text{ K}\}$, and $T_2 \in [289\text{ K}, 311\text{ K}]$.

B. NUC Based on a Staircase Scene

To validate the effectiveness of the proposed NUC method in point target detection systems, we established an imaging platform as illustrated in Fig. 4 to detect the airliners leaving from Changchun Longjia International Airport. A global navigation system 5890 USB-ADSB receiver was employed to pinpoint the geographic location of airliners, including longitude, latitude, and altitude. Besides, the International Civil Aviation Organization 24-bit address, identification, nation, speed, and type of aircrafts could be read out from the ADSB viewer. The IR camera was mounted on the FLIR motion control systems, which was connected with the PC through a RJ45 Ethernet connector. The pan position and tilt position of the camera could be changed with E-series pan-tilt units. The integration

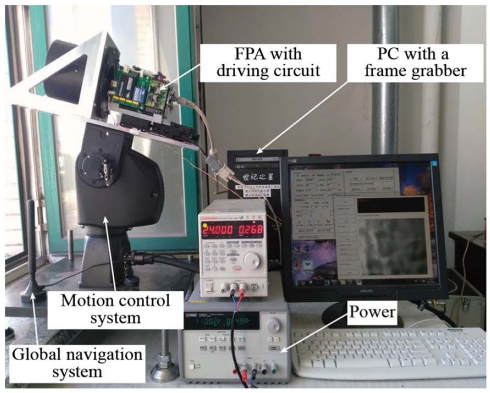

Fig. 4. Proof-of-concept point target detection system.

time was set to 600 μs to acquire half-well capacity. The whole experiment was performed in winter in Changchun.

To perform the NUC experiment based on a staircase scene, the camera was tilted to a fixed pitch angle of 20°. This angle was an experiential value, from which we were able to detect the airliners. Then, the camera was panned to the position where a visibly uniform scene filled the field of view (FOV). The corresponding scene was snapped as I_2'. To quantitatively evaluate the uniformity of the staircase scene, I_2' was corrected with the standard two-point calibration method. The corrected image was denoted as I_2''. The average value of the row-wise STD of t I_2'' was 7.13. Sequentially, the camera was panned left 15° without lapping over with image I_2'. We snapped the image to be corrected as I_3, of which the mean value was 8251.35. To perform the standard two-point calibration experiment, we selected two uniform images I_1 and I_2 in Subsection 3.A. The mean values were 7456.92 and 8243.78, respectively, and the latter one was very close to the mean value of I_3. Finally, calibration coefficients $k_{i,j}$ and $b_{i,j}$ were calculated with I_1 and I_2, and $k'_{i,j}$ and $b'_{i,j}$ were calculated with I_1 and I_2'. The coefficients of the two methods for column 10 are compared in Fig. 5, and Fig. 6 shows the comparison for rows 100 and 300.

From Fig. 5, for the standard two-point calibration method, $k_{i,10}$ fluctuates near 1 and $b_{i,10}$ fluctuates near 0. Besides, it is obvious that the shapes of $k_{i,10}$ and $b_{i,10}$ are effectively flat, showing no apparent trend with the row index. In contrast, according to the analysis in Subsection 2.D, $k'_{i,10}$ decreases and $b'_{i,10}$ increases with the row index. For some rows, for example, from row 135 to 150, $k'_{i,10}$ shows an increasing trend. This is because $k'_{i,10}$ follows a combined trend with s_i and $k_{i,10}$. For rows 135 to 150, the shape of $k'_{i,10}$ is dominated by the increase of $k_{i,10}$. From Fig. 6, we could find that $k'_{100,j}$ and $k'_{300,j}$ follow a similar trend to $k_{100,j}$ and $k_{300,j}$, respectively, which demonstrates the rationality of the approximation in Eq. (8). The experimental results accord well with the theoretical models presented in Subsection 2.C, though the

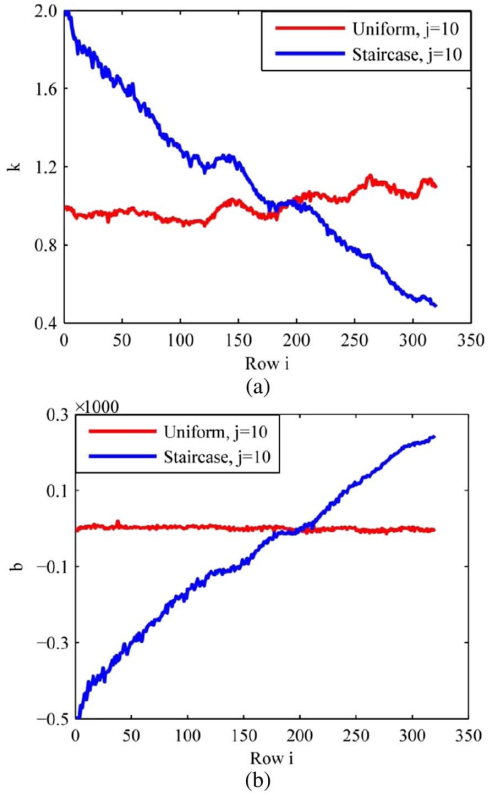

Fig. 5. Representative NUC coefficients (a) k and (b) b calculated with a uniform blackbody and a staircase scene when the column index j is fixed to 10.

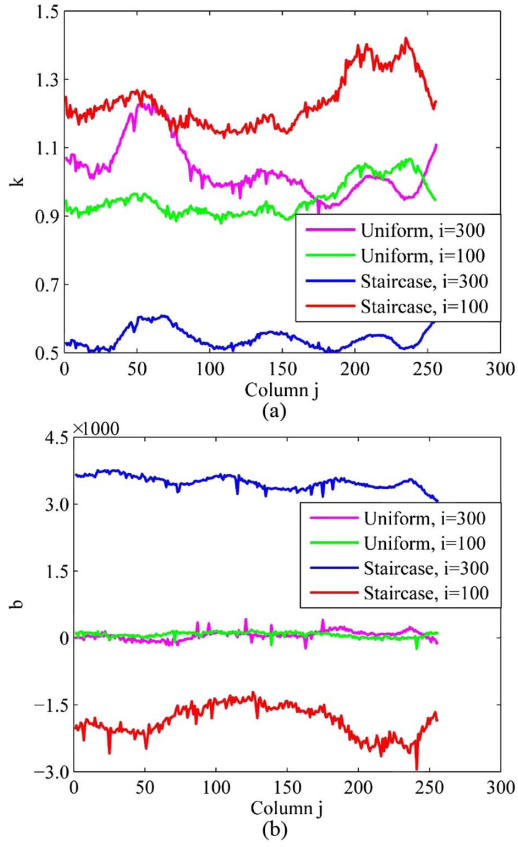

Fig. 6. Representative NUC coefficients (a) k and (b) b calculated with a uniform blackbody and a staircase scene when the row index i is fixed to 100 and 300, respectively.

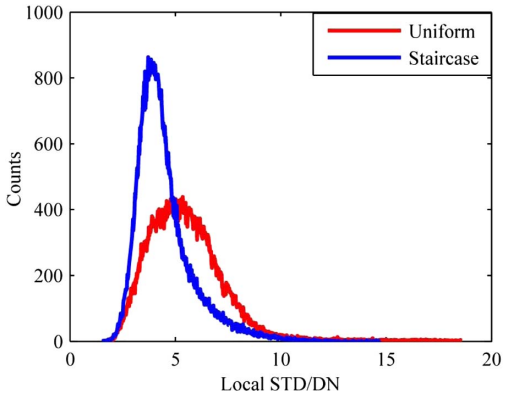

Fig. 7. Histogram of the local STD of the corrected image.

visibly uniform scene I_2' may not be perfectly uniform in the horizontal direction. A slight difference of the trend occurs due to the random noise inside the FPA. Similarly, $b'_{100,j}$ and $b'_{300,j}$ follow an inverse tread to $k'_{100,j}$ and $k'_{300,j}$, which is consistent with the analysis in Subsection 2.D.

In this practical experiment, as the scene is not uniform, global STD is not employed as a quantitative assessment. We did not estimate the background and then subtract it from the corrected image, because this introduces estimation errors. Instead, we compute the STD of each 5×5 pixel local area. This is reasonable because the target with a long distance often occupies less than 3×3 pixels, and the local STD is of more concern than the global STD. The histogram of the local STD for the corrected images is presented in Fig. 7. It shows that the local STD of the proposed method is smaller than the standard two-point method. To quantitatively evaluate the NUC results, the measurement was repeated 50 times independently, and the mean local STD of the two methods is plotted in Fig. 8. The proposed method outperforms the two-point standard method in terms of local STD.

C. Effect of the NUC Method on the Target SCR

To demonstrate the potential advantages of the proposed NUC method, we grabbed 2000 frames and detected three airliners with the established point target detection system. A screen

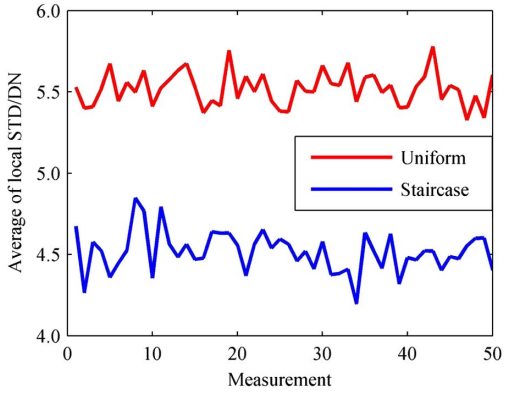

Fig. 8. Average of the local STD in the 50 independent measurements.

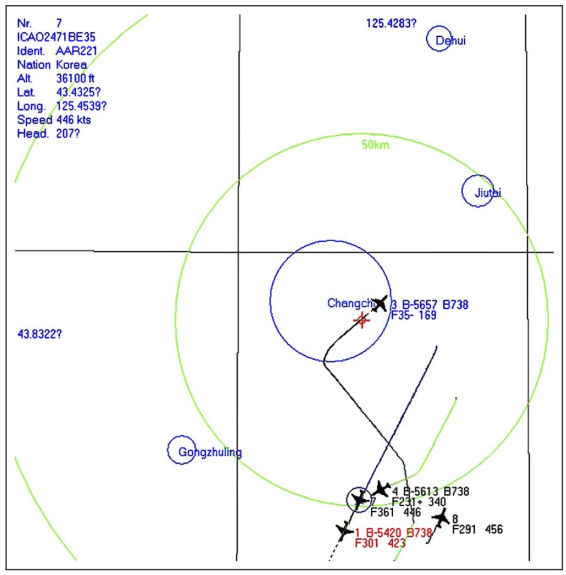

Fig. 9. Screen shot of the ADSB viewer. Airliners 1 (Boeing B738, 59.37 km away, from America), 4 (Boeing B738, 49.08 km away, from Singapore), and 7 (Airbus A340, 47.80 km away, from Korea) were in the FOV of frame 1407.

shot of the ADSB viewer is presented in Fig. 9. With the assistance of the ADSB receiver, we were able to find the three airliners manually in the sequential frames, and could calculate the distance between the airliners and the camera through the geodetic coordinate system. From frame 1396, the fourth airliner entered into the FOV. The raw frame 1407 and the corrected images are displayed in Fig. 10. To show the target more clearly, the 3D surfaces of the fourth airliner are illustrated in Fig. 11. For the fourth airliner, the radius r of the Airy disk is $r = 1.22\lambda F = 23.18$ μm, which approaches the pixel size of 30 μm [17]. Thus, the Airy disk occupies no more than four pixels in the FPA. When the center of the Airy disk coincides with the center of an individual detector element, the target occupies only one pixel. When the center of the Airy disk coincides with the vertex of an individual detector element, the target occupies four pixels.

Different from general imaging systems in which image contrast and dynamic range may be of more concern, the SCR of the point target is a crucial assessment in point target detection systems. Thus, we refer to the SCR of the point target to evaluate the effectiveness of the NUC method, which is defined as

$$\mathrm{SCR} = \frac{I_t - I_b}{\sigma_b}, \tag{13}$$

where I_t is the average of the target gray value. I_b and σ_b are the average and STD of the 5×5 pixel background with the same center as the target, respectively. With a higher SCR of the target, the detection system is capable of detecting targets further away with lower false alarm rate. The SCR of the target as a function of frame index is plotted in Fig. 12. We could see that the SCR result is generally consistent with the local STD plot in

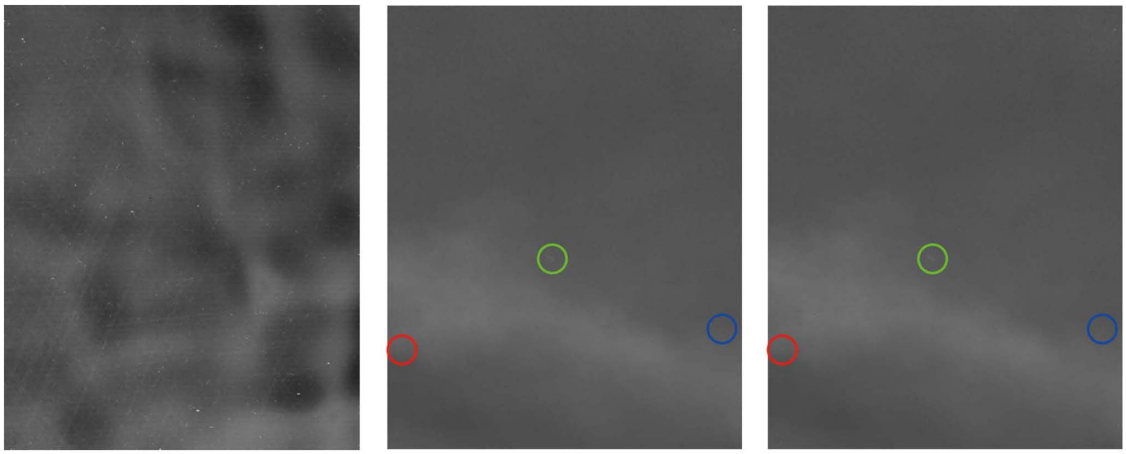

Fig. 10. Comparison of (a) raw frame 1407 and the corrected images with (b) blackbody and (c) staircase scene. The blue, red, and green circles correspond to airliners 1, 4, and 7, respectively. The targets are so small, and they may be much clearer in 3D surfaces as illustrated in Fig. 11.

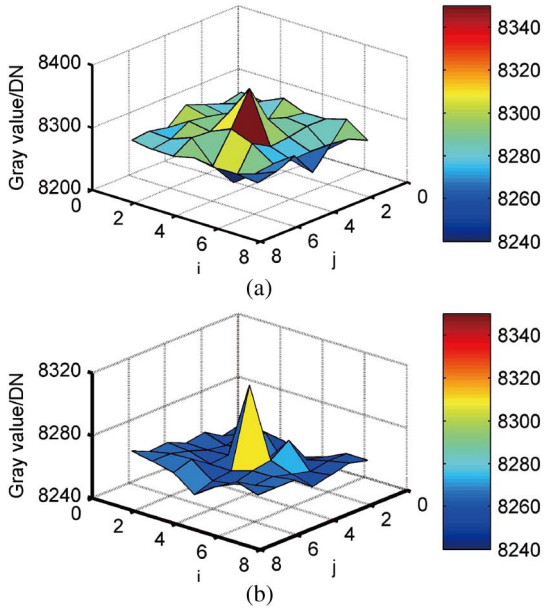

Fig. 11. Surface plot of the fourth airliner corrected with (a) blackbody and (b) staircase scene. The SCR of this target is 5.3 and 11.4, respectively.

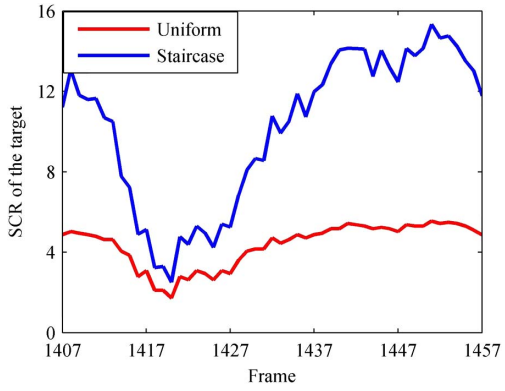

Fig. 12. SCR of the fourth airliner as a function of frame index.

Fig. 7. The proposed NUC method can effectively improve the target SCR.

4. CONCLUSION

In this paper, we developed a new NUC method based on staircase scenes for point target detection systems. We replaced one of the uniform scenes of the standard two-point calibration method with a staircase scene, which matches the intensities of the to-be-corrected image in a row-wise manner. The primary advantage of this approach is its high precision and compensation for the response nonlinearity of FPAs. Besides, like any other scene-based NUC method, the entire optical system can be calibrated without halting normal operations. The proposed NUC method can decrease the local STD of images in airborne IRST systems. Future extensions of this work may include picking out the staircase scene with the fewest clouds automatically among multiple frames, and updating NUC coefficients in extremely bad weather.

APPENDIX A

$\overline{I_1}$ and $\overline{I_2}$ are the mean values of images I_1 and I_2, given by

$$\begin{cases} \overline{I_1} = \overline{G} \cdot E_1 + \overline{O} \\ \overline{I_2} = \overline{G} \cdot E_2 + \overline{O}, \end{cases} \tag{A1}$$

where $\overline{G}$ and $\overline{O}$ are the average response and offset of all the detector elements in the FPA as follows:

$$\begin{cases} \overline{G} = \frac{1}{MN} \sum_{m=1}^{M} \sum_{n=1}^{N} G_{m,n} \\ \overline{O} = \frac{1}{MN} \sum_{m=1}^{M} \sum_{n=1}^{N} O_{m,n} \end{cases}. \tag{A2}$$

Here, E_1 and E_2 correspond to the energy incident on each detector element. $\overline{I'_2}$ is the mean value of I'_2. That is,

$$\overline{I'}_2 = \frac{1}{MN} \sum_{m=1}^{M} \sum_{n=1}^{N} [G_{m,n}(E_2 + \Delta E_m) + O_{m,n}]. \tag{A3}$$

For Eq. (7),

$$
\begin{aligned}
k'_{i,j} &= \frac{\overline{I'_2} - \overline{I_1}}{I'_{2,i,j} - I_{1,i,j}} = \frac{\frac{1}{MN}\sum_{m=1}^{M}\sum_{n=1}^{N} G_{m,n}(E_2 - E_1 + \Delta E_m)}{G_{i,j}(E_2 - E_1 + \Delta E_i)} \\
&= \frac{\frac{1}{MN}\sum_{m=1}^{M}\sum_{n=1}^{N} G_{m,n}(E_2 - E_1 + \Delta E_i + \Delta E_m - \Delta E_i)}{G_{i,j}(E_2 - E_1 + \Delta E_i)} \\
&= \frac{\overline{G}}{G_{i,j}} + \frac{\frac{1}{MN}\sum_{m=1}^{M}\sum_{n=1}^{N} G_{m,n}(\Delta E_m - \Delta E_i)}{G_{i,j}(E_2 - E_1 + \Delta E_i)} \\
&= \frac{\overline{G}}{G_{i,j}} + \frac{\frac{1}{M}\sum_{m=1}^{M}(\frac{1}{N}\sum_{n=1}^{N} G_{m,n})(\Delta E_m - \Delta E_i)}{G_{i,j}(E_2 - E_1 + \Delta E_i)}.
\end{aligned} \tag{A4}
$$

According to Eq. (6), Eq. (12) can be calculated as follows:

$$
\begin{aligned}
b'_{i,j} &= \overline{I}_1 - k'_{i,j} \cdot I_{1,i,j} \\
&= \overline{G} \cdot E_1 + \overline{O} - \frac{\overline{G}}{G_{i,j}}(1 + s_i)(G_{i,j} \cdot E_1 + O_{i,j}) \\
&= \overline{O} - \frac{\overline{G}}{G_{i,j}} O_{i,j} - \frac{\overline{G}}{G_{i,j}} \cdot s_i(G_{i,j} \cdot E_1 + O_{i,j}) \\
&= b_{i,j} - s_i \cdot \overline{G}\left(E_1 + \frac{O_{i,j}}{G_{i,j}}\right).
\end{aligned} \tag{A5}
$$

To analyze the monotonicity of s_i, assume that $E_2 > E_1$ and $i_2 > i_1$ without loss of generality. When $\Delta E_{i_2} > \Delta E_{i_1}$,

$$
\begin{aligned}
s_{i_2} - s_{i_1} &= \frac{\frac{1}{M}\sum_{m=1}^{M}(\Delta E_m - \Delta E_{i_2})}{E_2 - E_1 + \Delta E_{i_2}} - \frac{\frac{1}{M}\sum_{m=1}^{M}(\Delta E_m - \Delta E_{i_1})}{E_2 - E_1 + \Delta E_{i_1}} \\
&< \frac{\frac{1}{M}\sum_{m=1}^{M}(\Delta E_m - \Delta E_{i_2})}{E_2 - E_1 + \Delta E_{i_1}} - \frac{\frac{1}{M}\sum_{m=1}^{M}(\Delta E_m - \Delta E_{i_1})}{E_2 - E_1 + \Delta E_{i_1}} \\
&= \frac{\frac{1}{M}\sum_{m=1}^{M}(\Delta E_m - \Delta E_{i_2} - \Delta E_m + \Delta E_{i_1})}{E_2 - E_1 + \Delta E_{i_1}} \\
&= \frac{\frac{1}{M}\sum_{m=1}^{M}(\Delta E_{i_1} - \Delta E_{i_2})}{E_2 - E_1 + \Delta E_{i_1}} = \frac{\Delta E_{i_1} - \Delta E_{i_2}}{E_2 - E_1 + \Delta E_{i_1}} < 0.
\end{aligned} \tag{A6}
$$

That is, s_i keeps decreasing with the increase of row index i, regardless of the column index j. Similarly, we can come to the conclusion that $s_{i_2} - s_{i_1} > 0$ when $\Delta E_{i_2} < \Delta E_{i_1}$.

Funding. National Natural Science Foundation of China (NSFC) (61308099).

REFERENCES

1. A. F. Milton, F. R. Barone, and M. R. Kruer, "Influence of nonuniformity on infrared focal plane array performance," Opt. Eng. **24**, 855–862 (1985).
2. J. M. Mooney, F. D. Sheppard, W. S. Ewing, J. E. Ewing, and J. Silverman, "Responsivity nonuniformity limited performance of infrared staring cameras," Opt. Eng. **28**, 1151–1161 (1989).
3. D. L. Perry and E. L. Dereniak, "Linear theory of nonuniformity correction in infrared staring sensors," Opt. Eng. **32**, 1854–1859 (1993).
4. Z. Sun, S. Chang, and W. Zhu, "Radiometric calibration method for large aperture infrared system with broad dynamic range," Appl. Opt. **54**, 4659–4666 (2015).
5. S. Kim, "Two-point correction and minimum filter-based nonuniformity correction for scan-based aerial infrared cameras," Opt. Eng. **51**, 106401 (2012).
6. Y. Shi, T. Zhang, Z. Cao, and L. Hui, "A feasible approach for nonuniformity correction in IRFPA with nonlinear response," Infrared Phys. Technol. **46**, 329–337 (2005).
7. M. M. Hayat, S. N. Torres, E. Armstrong, S. C. Cain, and B. Yasuda, "Statistical algorithm for nonuniformity correction in focal-plane arrays," Appl. Opt. **38**, 772–780 (1999).
8. C. Zhang and W. Zhao, "Scene-based nonuniformity correction using local constant statistics," J. Opt. Soc. Am. A **25**, 1444–1453 (2008).
9. L. Geng, Q. Chen, and W. Qian, "An adjacent differential statistics method for IRFPA nonuniformity correction," IEEE Photon. J. **5**, 6801615 (2013).
10. R. C. Hardie, F. Baxley, B. Brys, and P. Hytla, "Scene-based nonuniformity correction with reduced ghosting using a gated LMS algorithm," Opt. Express **17**, 14918–14933 (2009).
11. B. Narayanan, R. C. Hardie, and R. A. Muse, "Scene-based nonuniformity correction technique that exploits knowledge of the focal-plane array readout architecture," Appl. Opt. **44**, 3482–3491 (2005).
12. J. Zeng, X. Sui, and H. Gao, "Adaptive image-registration-based nonuniformity correction algorithm with ghost artifacts eliminating for infrared focal plane arrays," IEEE Photon. J. **7**, 1–7 (2015).
13. R. C. Hardie, M. M. Hayat, E. Armstrong, and B. Yasuda, "Scene-based nonuniformity correction with video sequences and registration," Appl. Opt. **39**, 1241–1250 (2000).
14. C. Zuo, Q. Chen, G. Gu, and X. Sui, "Scene-based nonuniformity correction algorithm based on interframe registration," J. Opt. Soc. Am. A **28**, 1164–1176 (2011).
15. A. Rogalski, *Infrared Detectors*, 2nd ed. (CRC Press, 2012).
16. R. A. Leathers, T. V. Downes, and R. G. Priest, "Scene-based nonuniformity corrections for optical and SWIR pushbroom sensors," Opt. Express **13**, 5136–5150 (2005).
17. W. J. Smith, *Modern Optical Engineering*, 4th ed. (McGraw-Hill, 2008).